

Research Paper

Theoretical modeling of liquid film and force effects in a printed circuit heat exchanger

Su Won Lee ^a, Jae Hyun Choi ^b, SeockYong Lee ^c, HangJin Jo ^{a,b,*}^a Division of Advanced Nuclear Engineering, POSTECH, Pohang 790-784 Republic of Korea^b Department of Mechanical Engineering, POSTECH, Pohang 790-784 Republic of Korea^c Research Institute of Industrial Science and Technology, RIST, Pohang 790-784 Republic of Korea

ARTICLE INFO

ABSTRACT

Keywords:

Theoretical liquid film model
Printed circuit heat exchanger
 CO_2 flow condensation
Effect of body force on liquid film
Effect of working fluid's properties

Accurate modeling of liquid films is crucial in understanding heat transfer coefficient trends as they vary with working fluids and channel shapes. Although theoretical liquid film models exist for various channel shapes, none addresses CO_2 in a printed circuit heat exchangers (PCHE). In this study, we developed a theoretical CO_2 liquid film model in a PCHE using the conservation, momentum, and energy equations. The model considers the combined effects of shear, surface, and gravitational forces on the liquid film flow and accounts for the liquid film accumulation at the corners, thereby highlighting the high CO_2 surface tension and semicircular channel features. It was compared to volume of fluid (VOF) simulations and void fraction models. The developed model differed by approximately 9.9 % from the Wallis's void model and predicted well up to approximately 7.4 % from the liquid film calculated by VOF. It enabled the quantitative evaluation of not only the liquid film but also forces affecting it based on various variables. Furthermore, a correlation between the liquid film and heat transfer coefficient was established, thereby showing a difference of approximately 1–13 % compared to the convection-dominated heat transfer model. This indicated that majority of the liquid film exhibited a wavy-laminar flow, with heat transferring via convection. Finally, the liquid film distribution was analyzed for different working fluids, thereby revealing that the CO_2 film is approximately 20–30 % thinner and more evenly distributed than those of the refrigerants owing to the higher surface tension and lower gas density of CO_2 .

1. Introduction

The increasing CO_2 emissions owing to the rapid development of the energy industry pose global environmental, health, economic, and security challenges, thereby making it an urgent issue [1]. Among the various climate change mitigation strategies, CO_2 capture and storage system (CCSS) using cold energy from liquefied natural gas (LNG) or hydrogen have shown considerable promise [2], as they offer the advantage of CO_2 condensation without high-pressure compression [3]. This approach not only enhances economic feasibility by reducing compressor work but also prevents energy waste [4]. However, to utilize LNG cold energy under high-pressure and cryogenic conditions, or hydrogen cold energy under cryogenic conditions, a structurally stable heat exchanger is required as the condenser in a CCSSs. Printed circuit heat exchangers (PCHEs), which feature high heat transfer efficiency and structural integrity under civil conditions, are well-suited for this application [5–7].

Numerous researchers have analyzed the condensation heat transfer characteristics of PCHEs for use as condensers in cold energy applications [8–10]. Kwon et al. [8] conducted condensation experiments in the PCHE and found that condensation heat transfer correlations for circular channels predicted heat transfer coefficients with discrepancies greater than 50 % compared to the experimental results. Yoo and Nam [9] further emphasized the inadequacy of existing condensation heat transfer correlations for PCHEs, thereby attributing the discrepancies to variations in the channel shapes. Peng and Zhang [10] employed a volume of fluid (VOF) simulation to investigate the impact of distinct channel shapes on heat transfer coefficients and found considerable differences between circular and semicircular channels, which is attributed to their varying liquid-film distributions. While previous studies suggest that condensation heat transfer is considerably influenced by liquid film distribution, a comprehensive theoretical model for predicting the CO_2 liquid film distribution in PCHEs has yet to be developed. Additionally, the relationship between variations in boundary conditions and heat transfer coefficient trends has only been

* Corresponding author.

E-mail address: jhj04@postech.ac.kr (H. Jo).

Nomenclature		Γ	Reynolds number of liquid film [-]
A	Heat transfer area [m^2]	<i>Subscripts/Superscripts</i>	
D	Diameter [m]	b	bottom
f	Friction factor [-]	c	condensation
G	Mass flux [$\text{kg}/\text{m}^2\cdot\text{s}$]	fg	liquid-vapor
h	Specific enthalpy [kJ/kg]	h	Hydraulic
h	Heat transfer coefficient [$\text{W}/\text{m}^2\cdot\text{K}$]	i	in
k	Thermal conductivity [$\text{W}/\text{m}\cdot\text{K}$]	l	liquid
L	Heat transfer length [m]	t	top
\dot{m}	Mass flow rate [kg/s]	r	r-direction
P	Pressure [bar]	v	vapor
Re	Reynolds number [-]	w	wall
Q	Heat transfer rate [W]	x	x-direction
q''	Heat flux [W/m^2]	z	z-direction
T	Temperature [$^\circ\text{C}$]	<i>Abbreviations</i>	
U	Uncertainty [-]	ASME	American Society of Mechanical Engineers
u	Velocity to x- and r- directions [m/s]	CCSS	CO_2 capture and storage system
w	Velocity to z-direction [m/s]	LNG	Liquefied natural gas
x	Quality [-]	MAPE	Mean absolute percentage error
α	Void fraction [-]	OFS	Optical fiber sensor
δ	Liquid film thickness [m]	PCHE	Printed circuit heat exchanger
μ	Viscosity [$\text{Pa}\cdot\text{s}$]	REFPROP	Reference Fluid Thermodynamic and Transport Properties database
ρ	Density [kg/m^3]	RTD	Resistance temperature detector
τ	Shear force [Pa]		
θ	Angle [$^\circ$]		

qualitatively associated with changes in the liquid film distribution. Therefore, developing a model for semicircular channels is crucial to accurately predict the heat transfer coefficients of PCHEs.

Nusselt [11] first developed a theoretical liquid film model on the wall based on numerous assumptions: laminar flow, constant liquid properties, no interfacial shear force between the liquid and vapor, and conduction-dominated transport of liquid film. Based on these assumptions, the liquid film distribution was determined by the force and energy balances along the flow direction. Wen et al. [12] observed the difficulty of applying Nusselt's model to minichannels, such as those in PCHEs, wherein the surface force increases and radial flow considerably affects the liquid film. To address these limitations, Kim and Mudawar [13] proposed a theoretical liquid film model for minichannels, which accounted for the radial flows formed by gravitational and surface forces, and demonstrated that its heat transfer coefficient predictions corresponded with the experimental results. Ding et al. [14] developed a new liquid film model for square channels as existing models based on circular channels were unsuitable for square channels with corners, wherein the liquid condensed in the top and bottom regions and accumulated at the corners owing to surface force. Wang and Ming [15] developed a liquid film model for oval microchannels and suggested that the channel shapes with corners form thicker liquid films at the corners owing to the surface tension. These studies underscore the influence of channel shape on liquid film distribution, thereby highlighting the need for novel liquid film models for different channel shapes to accurately predict the heat transfer coefficient. Additionally, the physical properties of working fluids influence the liquid film characteristics. Liu et al. [16] analyzed the liquid film distributions of various working fluids using VOF simulations and found that R-134a formed the thickest film under similar boundary conditions owing to its lower gas velocity resulting from higher density. Despite having the thickest film, R-134a exhibited the highest heat transfer coefficient owing to its superior thermal conductivity.

In summary, conventional heat transfer correlations fail to accurately predict the PCHE heat transfer coefficients owing to the varying liquid film distributions influenced by the working fluids and channel

shapes. Numerous researchers [11–16] have developed liquid film models for different channel shapes to analyze the impact of the channel shape on liquid films. They observed that the liquid film distribution was affected by the channel shape and number of corners in triangular and square channels, which in turn influenced the heat transfer coefficient. However, no existing models predict liquid film distribution for semi-circular shapes, such as those in PCHEs, and accurately determining the liquid film distribution in semicircular channels with two corners remains a challenge for conventional liquid film models. Moreover, CO_2 exhibits a greater influence on surface and shear forces than refrigerants owing to its high surface tension and low gas density. This implies that even under similar conditions, the liquid film distribution and heat transfer coefficient vary based on the properties of the working fluids. Hence, a new CO_2 liquid film model for PCHE is crucial to accurately predict their heat transfer coefficients. In this study, we developed a novel theoretical liquid film model for CO_2 condensation in a semi-circular channel using the governing equations of conservation, momentum, and energy while considering the thin film on the top, cumulated film on the bottom, and meniscus at the corners. A code based on this model was developed and validated using VOF simulations and conventional void fraction models. The validated code was further used to analyze the liquid film trends and quantitatively assess the forces influencing its formation. Furthermore, a correlation between the liquid film thickness and heat transfer coefficient was established, and the liquid film formation was calculated for different working fluids to determine the impact of fluid properties, such as density and surface tension. The development of the liquid film models for semicircular channels is expected to facilitate the design of PCHE-type condensers for various applications, such as CCSS, air separation, freeze desalination, cold chain, and cryogenic power generation cycles.

2. Theoretical liquid film model of PCHE

Conventional condensation heat transfer correlations fail to accurately predict the heat transfer coefficients of PCHEs owing to differing liquid film distributions in semicircular and circular channels. To

analyze the quantitative heat transfer trends under varying boundary conditions and design a PCHE-type condenser, predicting the liquid film distribution in a PCHE is crucial. Consequently, we developed a theoretical liquid film model for semicircular channels to accurately predict the PCHE heat transfer coefficients. The geometry and coordinate systems of the liquid film model for the semicircular channel are illustrated in Fig. 1(a). Only half of the channel was analyzed owing to its symmetry along the centerline [17]. The model was developed by dividing the liquid film into three zones: the thin film on the top, accumulated film on the bottom, and meniscus at the corner. The Cartesian coordinate system (x , y , z) was used for the top region (represented by the red coordinates in Fig. 1(a)), whereas a cylindrical coordinate system (r , θ , z) was employed for the bottom and meniscus regions (represented by the yellow coordinates for the bottom and green coordinates for the meniscus, respectively, as shown in Fig. 1(a)). The model was developed using the conservation, momentum, and energy equations, thereby accounting for the influences of shear, surface, and gravitational forces on the liquid film flow. Shear force primarily affects the liquid film along the flow direction (z -direction), whereas surface tension and gravity affect the radial direction (x - and r -directions). The following assumptions were made for developing the model:

1. The liquid film is incompressible owing to the high density of the liquid CO_2 .
1. The liquid film exhibits laminar flow owing to its extremely low film thickness in PCHE resulting from a small channel diameter.
2. The interfacial shear, surface, and gravitational forces act only in the z -, x - and r -, and r -directions, respectively [18,19].
3. The effect of non-condensable gases was neglected as the interior of the test section was vacuumed using a vacuum pump.
4. The properties of the liquid and vapor phases were constant.

2.1. Thin film on top

$$f_v = 2 \left[\left(\frac{8}{Re_v} \right)^{12} + \frac{1}{\left[\left\{ -4 * 2^{0.5} \log_{10} \left[\left(\frac{6.9}{Re_v} \right)^{0.9} + \frac{\epsilon}{3.71 D_v} \right]^{16} + \left(\frac{37530}{Re_v} \right)^{16} \right\}^{16} \right]^{\frac{3}{2}}} \right]^{1/12} \quad (10)$$

For the thin film on the top, a Cartesian coordinate system was applied, with velocities in the x - and z -directions expressed as u_x and w_z , respectively. Based on Assumption 3, u_x is affected by the surface force and w_z is affected by the shear force [19]. The gravitational force was neglected as it neither impacts u_x nor w_z at the top [20]. The liquid film behavior on the top was determined using the following conservation, momentum, and energy equations:

Conservation equation:

$$dm = dm_c - dm_x - dm_z = \rho_l^* (d\delta^* dx^* dz) \quad (1)$$

where m_c represents the liquid mass condensed via heat transfer, and m_x and m_z represent the mass moved in the x - and z -directions under surface and shear forces, respectively. The remaining mass within the control volume was calculated as the difference between m_c and sum of m_x and m_z . The liquid mass exiting in the x - and z -directions was

calculated using the velocity profiles from the momentum equation as follows:

Momentum equation along the x - and r -directions:

Governing equation:

$$\mu_l \frac{\partial^2 u_x}{\partial y^2} - \frac{\partial p_{ls}}{\partial x} = 0 \quad (2)$$

$$\begin{aligned} \frac{\partial p_{ls}}{\partial x} &= \frac{\partial}{\partial x} \left(p_v - \frac{\sigma}{R} \right) \\ &= \frac{\partial}{\partial x} \left(p_v - \frac{\sigma \left\{ \left[1 + \left(\frac{\partial \delta}{\partial x} \right)^2 \right] \frac{\partial^2 \delta}{\partial z^2} - 2 \frac{\partial \delta}{\partial x} \frac{\partial \delta}{\partial z} + \left[1 + \left(\frac{\partial \delta}{\partial z} \right)^2 \right] \frac{\partial^2 \delta}{\partial x^2} \right\}}{\left[1 + \left(\frac{\partial \delta}{\partial z} \right)^2 + \left(\frac{\partial \delta}{\partial x} \right)^2 \right]^{3/2}} \right) \end{aligned} \quad (3)$$

$$\mu_l \frac{\partial^2 w_z}{\partial y^2} - \frac{\partial p}{\partial z} = 0 \quad (4)$$

Boundary conditions (B.C.) from no-slip and interfacial shear force:

$$u_x(0) = 0 \text{ (no-slip)} \frac{\partial u_x}{\partial y} \Big|_{y=\delta} = 0 \text{ (interfacial shear force)} \quad (5)$$

$$w_z(0) = 0 \text{ (no-slip)} \mu_l \frac{\partial w_z}{\partial y} \Big|_{y=\delta} = \tau \text{ (interfacial shear force)} \quad (6)$$

Velocity profile:

$$u_x(y) = \frac{1}{\mu_l} \left(\frac{\partial p_{ls}}{\partial x} \right) \left(\delta y - \frac{1}{2} y^2 \right) \quad (7)$$

$$w_z(y) = \frac{1}{2\mu_l} \left(\frac{\partial p}{\partial z} \right) y^2 + \left\{ \tau + \frac{1}{\mu_l} \left(\frac{\partial p}{\partial z} \right) \delta \right\} y \quad (8)$$

$$\tau = \frac{1}{2} f_v \rho u_v^2 \quad (9)$$

Mass transport:

$$dm_x = \rho_l \frac{\partial}{\partial x} \left\{ \int_0^\delta u_x(y) dy \right\} = \rho_l \frac{\partial}{\partial x} \left\{ \frac{\delta^3}{3\mu_l} \left(\frac{\partial p_{ls}}{\partial x} \right) \right\} \quad (11)$$

$$dm_z = \rho_l \frac{\partial}{\partial z} \left\{ \int_0^\delta w_z(y) dy \right\} = \rho_l \frac{\partial}{\partial z} \left\{ \left(\frac{\partial p}{\partial z} \right) \left(\frac{\delta^3}{3\mu_l} \right) + \frac{\tau \delta^2}{2} \right\} \quad (12)$$

where u_x and w_z represent the liquid film velocity profiles along the x - and z -directions, respectively, which are affected by shear and surface forces. $\frac{\partial p_{ls}}{\partial x}$ and $\frac{\partial p}{\partial z}$ represent the pressure gradients in the x - and z -directions, owing to the surface tension and shear forces, respectively [21]. The velocity profiles, u_x and w_z , were calculated using the governing equations and boundary conditions expressed in Eqs. (2)–(12).

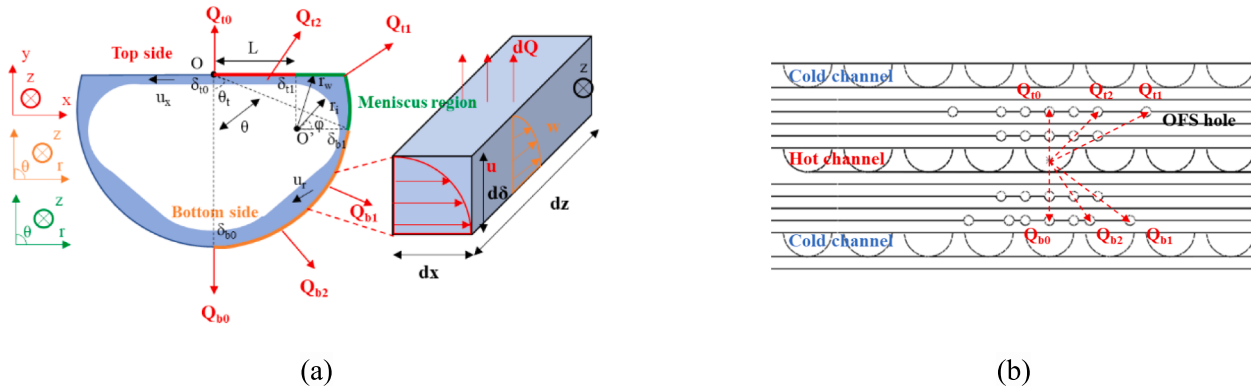


Fig. 1. (a) Illustration of a liquid film in PCHE and (b) schematic of the PCHE [17].

The mass flow rates were calculated by integrating the velocity profiles from the wall to the liquid film thickness.

The mass (m_c) condensed from gas to liquid was calculated using the following energy-balance equation:

$$dQ = dm_c * h_{fg} \quad (13)$$

where Q and h_{fg} denote the heat transfer rate from the hot to cold channel and latent heat of the working fluid, respectively. Q was measured along to the axial and radial directions through the OFS [17]. The liquid film distribution on the top was calculated by integrating the conservation, momentum, and energy equations as follows:

$$\begin{aligned} dm &= \frac{dQ}{h_{fg}} - \rho_l \frac{\partial}{\partial x} \left\{ \frac{\delta^3}{3\mu_l} \left(\frac{\partial p_{ls}}{\partial x} \right) \right\} - \rho_l \frac{\partial}{\partial z} \left\{ \left(\frac{\partial p}{\partial z} \right) \left(\frac{\delta^3}{\mu_l} \right) + \frac{\tau \delta^2}{2} \right\} \\ &= \rho_l * (d\delta * dx * dz) \end{aligned} \quad (14)$$

2.2. Accumulated film on bottom

A cylindrical coordinate system was employed to calculate the properties of the liquid film accumulated at the bottom [22], with velocities in the r - and z -directions denoted as u_r and w_z , respectively. Based on Assumption 3, u_r is influenced by the surface and gravitational forces, which vary with the angle between the normal vector of the wall and y -axis. As presented in Section 2.1, w_z is determined by the shear force. The liquid film behavior in the radial direction is expressed using the following equation:

Conservation equation:

$$dm = dm_c - dm_r - dm_z = \rho_l * (d\delta * rd\theta * dz) \quad (15)$$

The change in the control volume mass is calculated similarly to that described in Section 2.1. m_r denotes the mass moving in the r -direction owing to the surface tension and gravitational forces, whereas m_z represents that mass moving in the z -direction owing to the shear force.

Momentum equation along the r - and z -directions:

Governing equation:

$$\mu_l \left\{ \frac{\partial}{\partial r} \left[\frac{1}{r} \frac{\partial}{\partial r} (ru_r) \right] \right\} - \frac{1}{r} \left(\frac{\partial p_{ls}}{\partial \theta} \right) + (\rho_l - \rho_g) g \sin(\theta) = 0 \quad (16)$$

$$\frac{\partial p_{ls}}{\partial \theta} = \frac{\partial}{\partial \theta} \left(p_v - \frac{\sigma}{R} \right) = \frac{\partial}{\partial \theta} \left(p_v - \sigma - \frac{\delta^2 - \delta \frac{\partial^2 \delta}{\partial \theta^2} - \delta^3 \frac{\partial^2 \delta}{\partial z^2} + 2 \left(\frac{\partial \delta}{\partial \theta} \right)^2 - \delta \left(\frac{\partial \delta}{\partial \theta} \right)^2 \frac{\partial^2 \delta}{\partial z^2} + \delta^2 \left(\frac{\partial \delta}{\partial z} \right)^2 \frac{\partial^2 \delta}{\partial \theta^2} + 2\delta \left(\frac{\partial \delta}{\partial z} \right) \left(\frac{\partial \delta}{\partial \theta} \right) \left(\frac{\partial^2 \delta}{\partial z \partial \theta} \right)}{\delta^2 + \left(\frac{\partial \delta}{\partial \theta} \right)^2 + \delta^2 \left(\frac{\partial \delta}{\partial z} \right)^2} \right)^{3/2} \right) \quad (17)$$

$$\mu_l \left[\frac{1}{r} \frac{\partial}{\partial r} (r \frac{\partial w_z}{\partial r}) \right] - \frac{\partial p}{\partial z} = 0 \quad (18)$$

B.C. from no-slip and interfacial shear force:

$$u_r(r_w, \theta) = 0 \text{ (no-slip)} \Big|_{r=r_i} = 0 \text{ (interfacial shear force)} \quad (19)$$

$$w_z(r_w, \theta) = 0 \text{ (B.C. from no-slip)} \mu_l \frac{\partial w_z}{\partial y} \Big|_{r=r_i} = \tau \quad (20)$$

Velocity profile:

$$\begin{aligned} u_r(r, \theta) &= \frac{1}{3\mu_l} \left[\frac{1}{r} \left(\frac{\partial p_{ls}}{\partial \theta} \right) - (\rho_l - \rho_g) g \sin(\theta) \right] * \left\{ r^2 - r_i \left[\frac{2 + \left(\frac{r_w}{r_i} \right)^3}{1 + \left(\frac{r_w}{r_i} \right)^2} \right] r \right. \\ &\quad \left. + r_w^2 r_i \left[\frac{2 - \frac{r_w}{r_i}}{1 + \left(\frac{r_w}{r_i} \right)^2} \right]^* \frac{1}{r} \right\} \end{aligned} \quad (21)$$

$$w_z(r, \theta) = \frac{1}{4\mu_l} \left(\frac{\partial p}{\partial z} \right) \left[r^2 - 2r^2 \ln \left(\frac{r}{r_w} \right) - r_w^2 \right] - \frac{\tau r_i}{\mu_l} \ln \left(\frac{r}{r_w} \right) \quad (22)$$

Mass transport:

$$\begin{aligned} dm_r &= \rho_l \frac{\partial}{\partial \theta} \left\{ \int_{r_i}^{r_w} u_r(r, \theta) dr \right\} \\ &= \frac{\rho_l}{\mu_l r_i} \left[((\rho_l - \rho_g) g) \frac{\partial}{\partial \theta} (f_1 * \sin(\theta)) + \frac{\partial}{\partial \theta} \left(f_2 * \frac{\partial p_{ls}}{\partial \theta} \right) \right] \end{aligned} \quad (23)$$

$$dm_z = \rho_l \frac{\partial}{\partial z} \left\{ \int_{r_i}^{r_w} r * w_z(r, \theta) dr \right\} = \frac{\rho_l}{\mu_l r_i} \left[\frac{\partial}{\partial z} (tf_3 + \frac{\partial}{\partial z} \frac{\partial p}{\partial z} f_4) \right] \quad (24)$$

$$\begin{aligned} f_1 &= \frac{r_3}{18} + \frac{7}{36} r_i^3 - \frac{r_w r_i^2}{6} \left(1 + \frac{1}{2} \left(\frac{r_i}{r_w} \right)^3 \right) - \frac{r_i^3}{6} \ln \left(\frac{r_w}{r_i} \right) f_2 \\ &= \frac{r_i^2}{2} \ln \left(\frac{r_w}{r_i} \right) + \frac{r_w^2}{8} \left(\left(\frac{r_i}{r_w} \right)^4 - 1 \right) f_3 = -\frac{r_i^3}{4} + \frac{r_i r_w^2}{4} - \frac{r_i^3}{2} \ln \left(\frac{r_w}{r_i} \right) f_4 \\ &= -\frac{r_w^4}{16} - \frac{3r_i^4}{16} + \frac{r_i^2 r_w^2}{4} + \frac{r_i^4}{4} \ln \left(\frac{r_i}{r_w} \right) \end{aligned} \quad (25)$$

In contrast to the film on the top, u_r of the film accumulated on the bottom is influenced by the gravitational force and the effect varies by

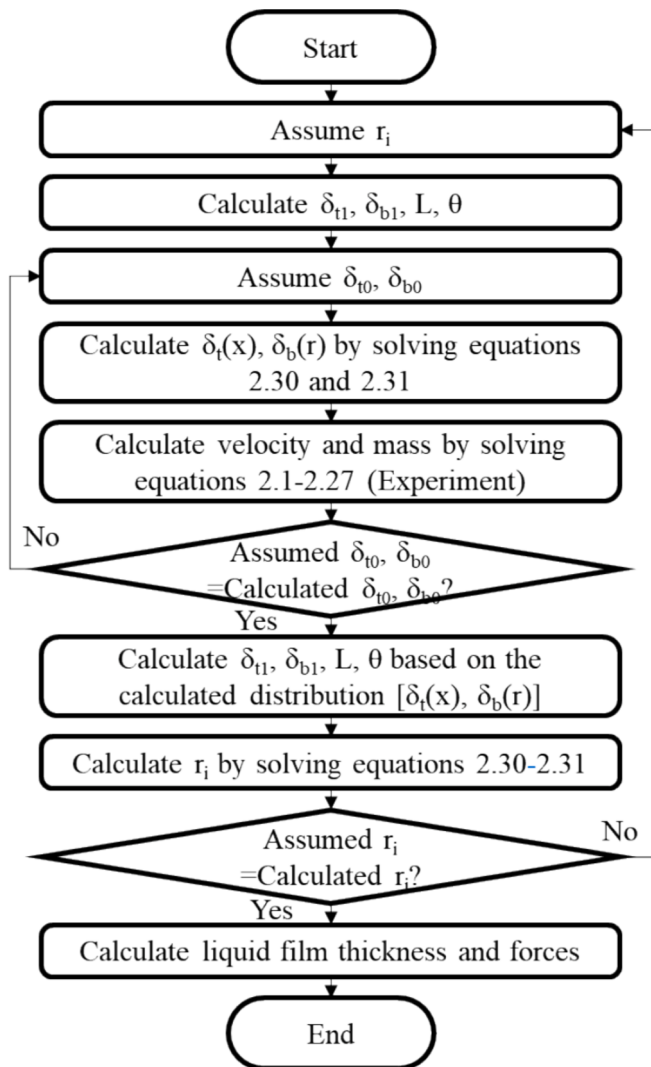
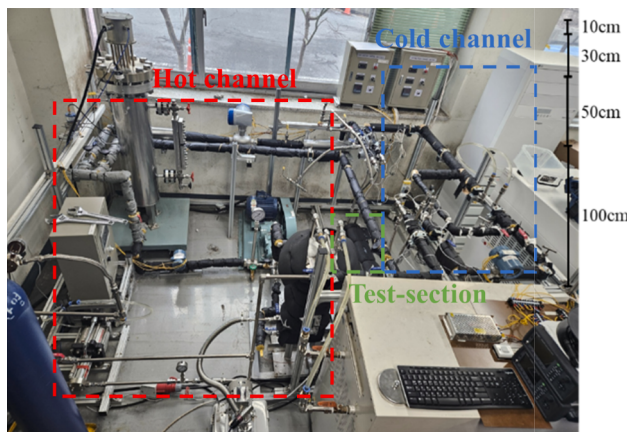
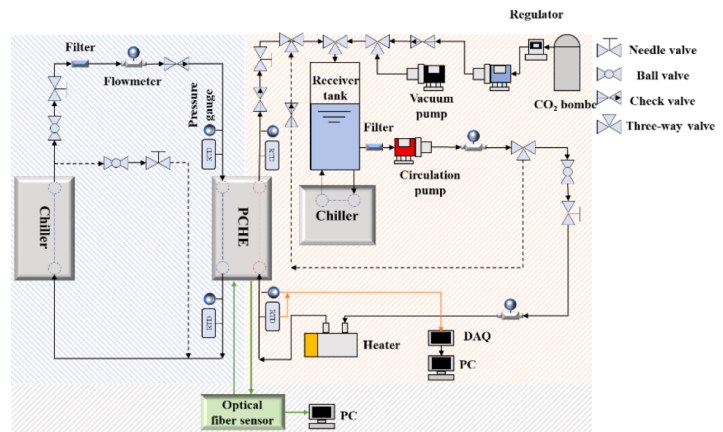


Fig. 2. Flowchart of the liquid film distribution calculation process.



(a)



(b)

Fig. 3. Experimental facility [17]: (a) photograph and (b) schematic.

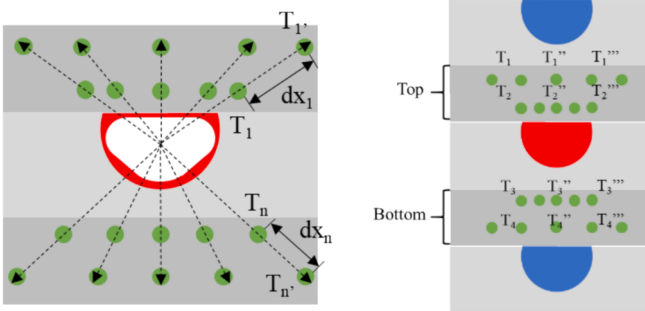


Fig. 4. Calculation methodologies of heat transfer rate.

The mass, momentum, and energy of the liquid film at the top are calculated as follows:

$$dm = \frac{dQ}{h_{fg}} + \frac{\rho_l}{\mu_l r_i} \left[-((\rho_l - \rho_g)g) \frac{\partial}{\partial \theta} (f_1(\theta) * \sin(\theta)) + \frac{\partial}{\partial \theta} \left(f_2(\theta) * \frac{\partial p_{ls}}{\partial \theta} \right) \right] + \rho_l \frac{\partial}{\partial x} \left\{ \frac{\delta^3}{3\mu_l} \left(\frac{\partial p_{ls}}{\partial x} \right) \right\} - \frac{\rho_l}{\mu_l r_i} \left[\frac{\partial}{\partial z} (r f_3(\theta)) + \frac{\partial}{\partial z} \left(\frac{\partial p}{\partial z} f_4(\theta) \right) \right] = \rho_l * (d\delta * rd\theta * dz) \quad (29)$$

2.4. Numerical calculation procedure

To determine the liquid film distribution, the equations expressed in the aforementioned sections were derived analytically using conservation, momentum, and energy equations. The heat transfer rate at each point was measured using the OFS in the radial and axial directions to obtain the energy equation [17]. Additionally, the liquid film function based on the positions ($\frac{\partial p_{ls}}{\partial x}$, $\frac{\partial p_{ls}}{\partial \theta}$) was calculated using the boundary conditions (Eqs. (30) and (31)), which were derived from the symmetry and continuity of the interfacial slope and curvature at the junction between the thin film and meniscus region [23,24]. In the x- and r-directions, the liquid films on the top and bottom were approximated as fourth-order functions of x (or r) as follows:

B.C. from symmetry conditions at the top and bottom:

$$\delta_t(0) = \delta_{t0}, \delta_t(L) = \delta_{t1}, \left. \frac{\partial \delta_t}{\partial x} \right|_{x=0} = 0, \left. \frac{\partial \delta_t}{\partial x} \right|_{x=L} = 0 \quad (30)$$

$$\delta_b(0) = \delta_{b0}, \delta_b(\theta) = \delta_{b1}, \left. \frac{\partial \delta_b}{\partial \theta} \right|_{\theta=0} = 0, \left. \frac{\partial \delta_b}{\partial \theta} \right|_{\theta=\theta_t} = 0 \quad (31)$$

A numerical solver was developed in MATLAB and the physical

properties of the working fluid were calculated using the reference fluid thermodynamic and transport property database (REFPROP). The liquid film distribution was calculated using the flowchart shown in Fig. 2 by employing the analytically developed model and heat transfer rates measured via the OFS in the experiment. The detailed procedure is as follows:

1. Assume r_i for the meniscus region and calculate the corresponding values of δ_{t0} , δ_{b0} , L , and θ .
2. Assume δ_{t0} and δ_{b0} at the center of the top and bottom regions, respectively.
3. Using the assumptions in Steps 1 and 2, calculate $\delta(x)$ and $\delta(r)$ based on the boundary conditions obtained using Eqs. (30) and (31).
4. Calculate the velocities, mass, and forces of the film in the top and bottom regions using Eqs (1)–(27).
5. Iterate until the assumed values (δ_{t0} and δ_{b0}) converge with those derived from the forces and heat transfer rates (Q_{t0} and Q_{b0}) in the

experiment.

6. Calculate the liquid-film distribution and mass in the x- and r-directions for the top and bottom regions. Determine r_i in the meniscus region using Eqs. (30) and (31) and the heat-transfer rate (Q_{t1}).
7. Repeat the calculations until r_i value assumed in Step 1 corresponds with that calculated through Steps 1–6.

This procedure was used to calculate the liquid film thickness distribution and forces acting on the film as a function of quality.

3. Experimental facility and data reduction

To calculate the liquid film distribution, the heat transfer rates of the energy equation in the radial and axial directions were required. Hence, an experimental facility was developed to determine the heat transfer rate distribution as shown in Fig. 3 [17]. This facility comprised hot and cold sides, with CO₂ and water–ethylene glycol mixtures employed as the working fluids, respectively. The OFS, which offers various advantages such as high sensitivity, small size, flexibility, and multiplexed sensing, was used to measure the heat transfer rate distribution [25]. The PCHE was manufactured using diffusion bonding and chemical

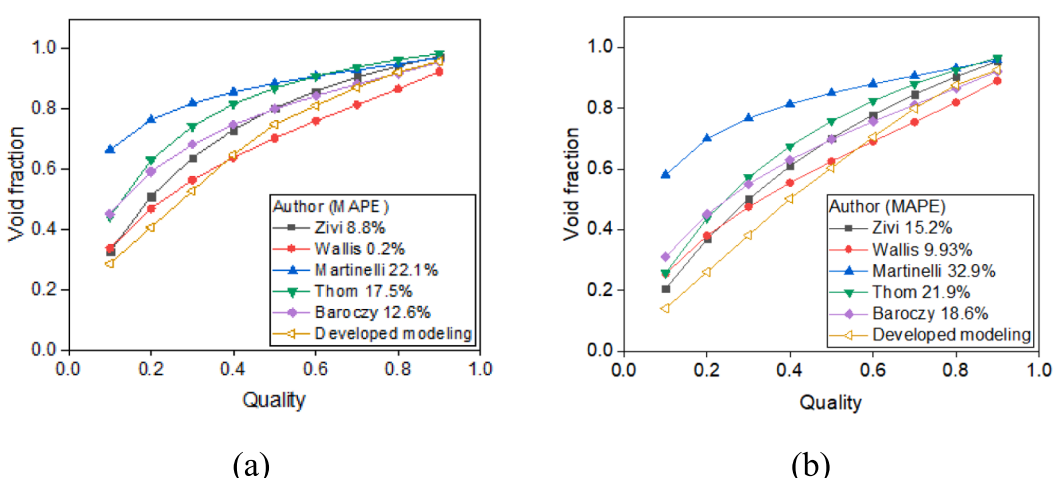


Fig. 5. Comparisons of void fraction models [27–29] at pressures of (a) 40 bar (b) 60 bar.

Table 1

Conventional void fraction models [27–29].

Author	Void fraction models	Boundary conditions
Zivi	$\alpha = \left[1 + \left(\frac{1-x}{x} \right) \left(\frac{\rho_v}{\rho_l} \right)^{0.67} \right]^{-1}$	Steam-water in horizontal and vertical macro-channels (annular flow)
Wallis	$\alpha = \left[1 + \left(\frac{1-x}{x} \right)^{0.72} \left(\frac{\rho_v}{\rho_l} \right)^{0.4} \left(\frac{\mu_l}{\mu_v} \right)^{0.08} \right]^{-1}$	Refrigerants and steam-water in horizontal minichannels (annular, wavy, slug, and bubbly flow)
Martinelli	$\alpha = \left[1 + 0.28 \left(\frac{1-x}{x} \right)^{0.64} \left(\frac{\rho_v}{\rho_l} \right)^{0.36} \left(\frac{\mu_l}{\mu_v} \right)^{0.07} \right]^{-1}$	Air, steam-water in minichannels
Thom	$\alpha = \left[1 + \left(\frac{1-x}{x} \right) \left(\frac{\rho_v}{\rho_l} \right)^{0.89} \left(\frac{\mu_l}{\mu_v} \right)^{0.18} \right]^{-1}$	Refrigerants in circular minichannels (laminar and turbulent flows)
Baroczy	$\alpha = \left[1 + \left(\frac{1-x}{x} \right)^{0.74} \left(\frac{\rho_v}{\rho_l} \right)^{0.65} \left(\frac{\mu_l}{\mu_v} \right)^{0.13} \right]^{-1}$	Refrigerants in macro-channels

etching. To ensure structural safety, its pitch and thickness values for different channel diameters (2, 3, and 4 mm) were determined using the American Society of Mechanical Engineers (ASME) standard [26]. Appendix A shows the detailed geometry of the PCHE. The physical properties of the working fluids used in the energy equations were obtained from REFPROP.

The heat flux in the radial and axial directions was calculated using the conduction equation [31] and wall temperatures measured by the OFS as shown in Fig. 4. The heat transfer rate (Q) was calculated as the product of the heat flux (q'') and the heat transfer area (A), wherein A is derived as the product of the diameter (D_{OFS}) and length (L). The heat transfer rates in the radial- and axial-directions were calculated as follows:

Heat flux:

$$q''_n = \frac{(T_n - T_w)}{dx_n} \quad (29)$$

Heat-transfer rate:

$$Q_n = q''_n * A = q''_n * (D_{OFS} * L) \quad (30)$$

To validate experimental results, verifications of the experimental facility and measurement methodology were conducted in a previous study [17]. The heat transfer rates measured in the hot and cold channels showed a difference of 2–8 %. The overall heat transfer coefficient and friction factor obtained from the experiment approximately 7.4 % and 7.3 %, respectively, than the correlations commonly used in the PCHE. These findings confirm that experimental facility accurately predicts the thermal-hydraulic performance. Additionally, the temperature distributions calculated in experiments and COMSOL simulations

were compared, thereby revealing a difference of approximately 0.1–0.2 °C. Based on these results, the temperature distribution and heat transfer rate predictions are reasonable.

4. Validation of developed liquid film model in PCHE

To validate the developed liquid film model in the PCHE, its void fraction predictions were compared to those of conventional void fraction models [27–29]. The void fraction represents the volume occupied by gas phase relative to the total volume. Conventional void fraction models generally calculate the average gas amount in one plane and can be applied to some extent without considering the characteristics of CO₂ and PCHE. Fig. 5 shows the void fractions calculated as a function of quality, wherein the empty yellow triangles represent the void fractions calculated using the proposed model, whereas the others represent those calculated using the conventional void fraction models (Table 1). Among the conventional models, the Wallis model predictions were the closest to those of the proposed model, with the mean average percentage error (MAPE) of 9.93 %. Wallis's void fraction model was developed for minichannels, which is similar to the PCHE, using water and a refrigerant as the working fluids while considering various flow patterns. This suggests that the density and viscosity ratios of CO₂ under different phases are between those of water and the refrigerant. Since it was developed for minichannels, it can be assumed to correspond with the CO₂ characteristics and PCHE. Furthermore, the liquid film distribution predicted by the model was compared to that obtained from the VOF simulation [10], as shown in Fig. 6, thereby revealing their difference of 5.08–7.44 %. This indicates that the liquid film distribution calculated using the developed model accurately captures the condensed liquid based on quality.

5. Results and analysis

In this study, we developed a novel liquid film model to quantitatively evaluate the effects of various forces on liquid film formation. The gravitational, shear, and surface tension forces are influenced by factors such as the channel diameter, mass flux, and saturation pressure, respectively. Mass flux alters the velocities of gases and liquids, thereby influencing the interfacial shear force and liquid film thickness. Saturation pressure influences the physical properties of CO₂ such as gas density and surface tension, which affect the shear and surface forces. Previous studies [14] have reported that the influence of gravitational force diminishes as the channel diameter owing to the minimal mass of the liquid condensed in small channels. To evaluate the effects of these forces on the liquid film, an analysis was conducted by varying the

Table 2
Operating conditions of the experiment.

Working fluids	CO ₂	Ethylene glycol
G [kg/m ² ·s]	40 ~ 80	~1,000
P _s [bar]	40 ~ 60	~8
D [mm]	2 ~ 4	

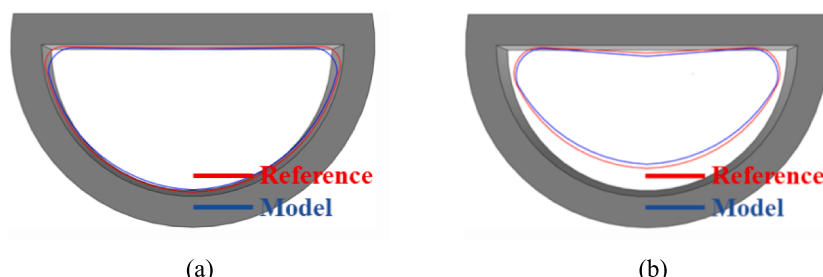


Fig. 6. Comparisons of liquid films with that developed in a previous study [10] of qualities (a) 0.8 and (b) 0.4.

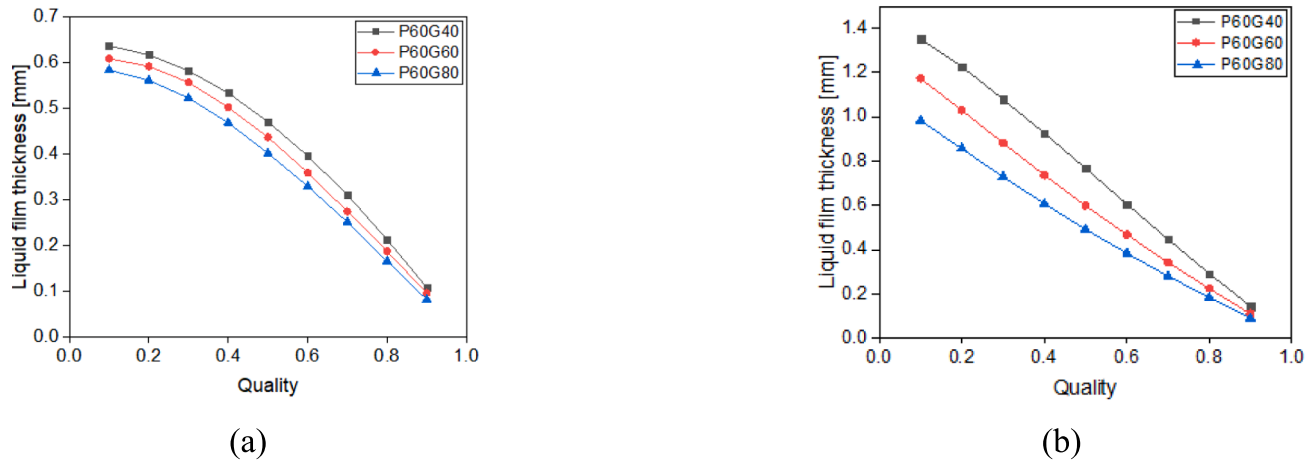


Fig. 7. Variations in liquid film thickness with mass flux (a) top and (b) bottom.

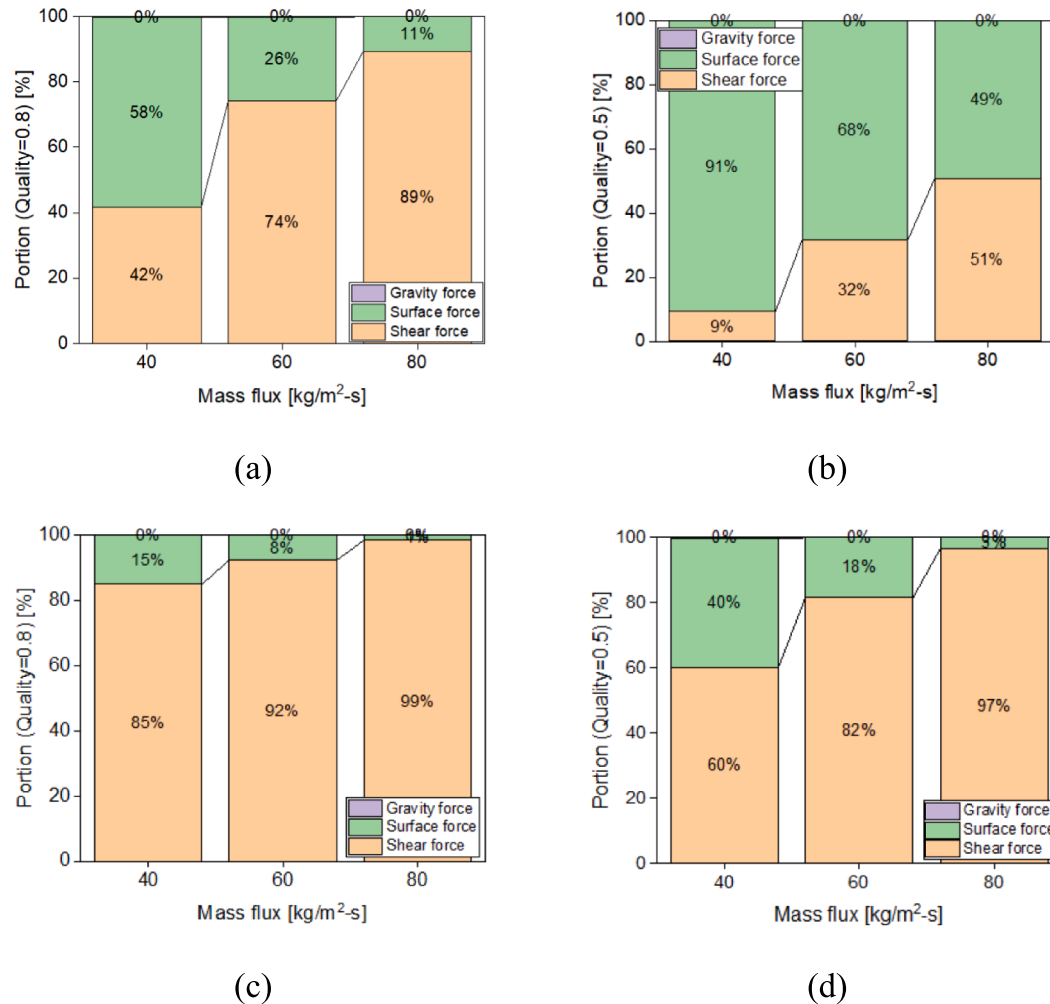


Fig. 8. Variation in forces acting on thin film with respect to mass flux: Top film under qualities of (a) 0.8 and (b) 0.5; bottom film under qualities of (c) 0.8 and (d) 0.5.

aforementioned variables, with the boundary conditions presented in Table 2. An analysis was performed at the central points of the top and bottom regions of the film to ease understanding.

5.1. Effect of mass flux on liquid film

Fig. 7 illustrates the relationship between the liquid film thickness and mass flux. Here, the thickness increases as the quality decreases because a greater quantity of gas condenses into the liquid at lower quality levels. As shown in the figure, the thickness decreases as the

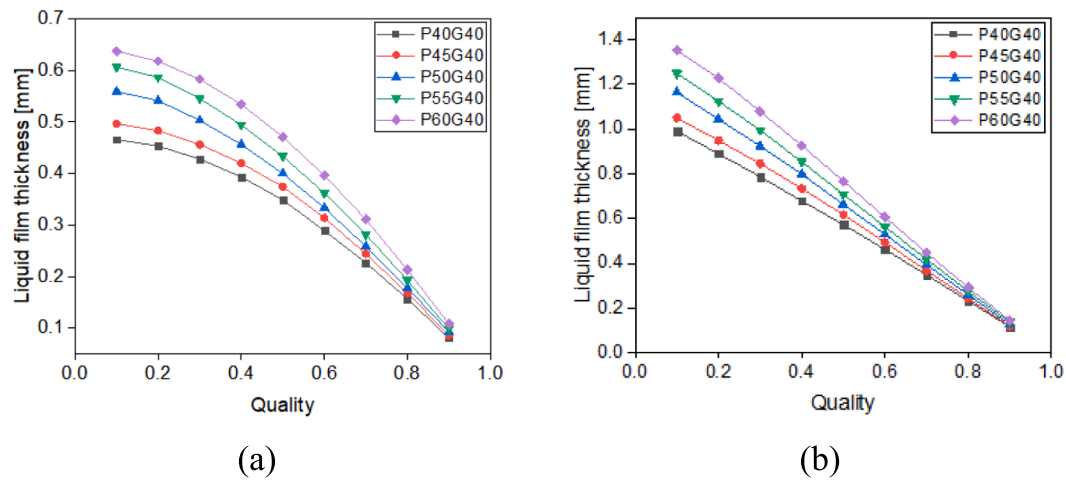


Fig. 9. Liquid film thickness under various saturation pressures: (a) top and (b) bottom.

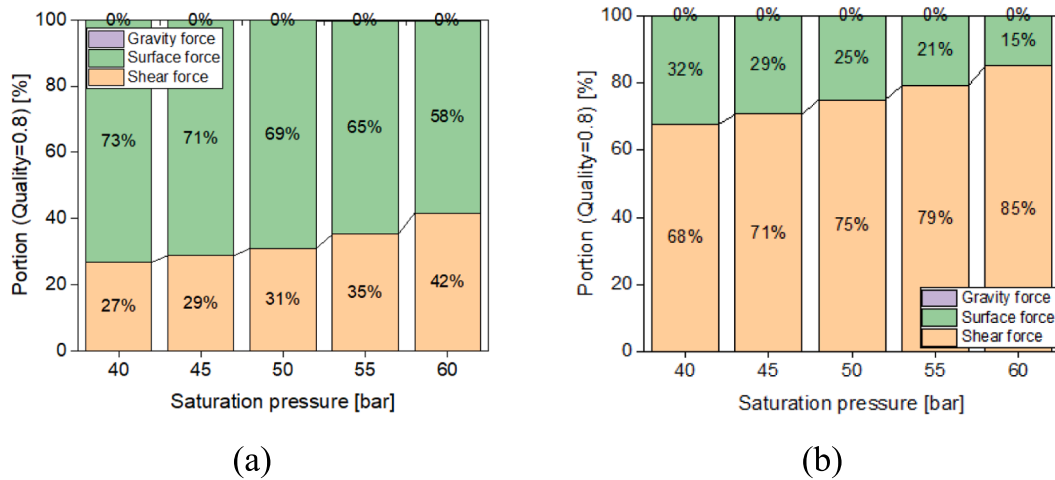


Fig. 10. Variation in forces under different saturation pressures: (a) top and (b) bottom.

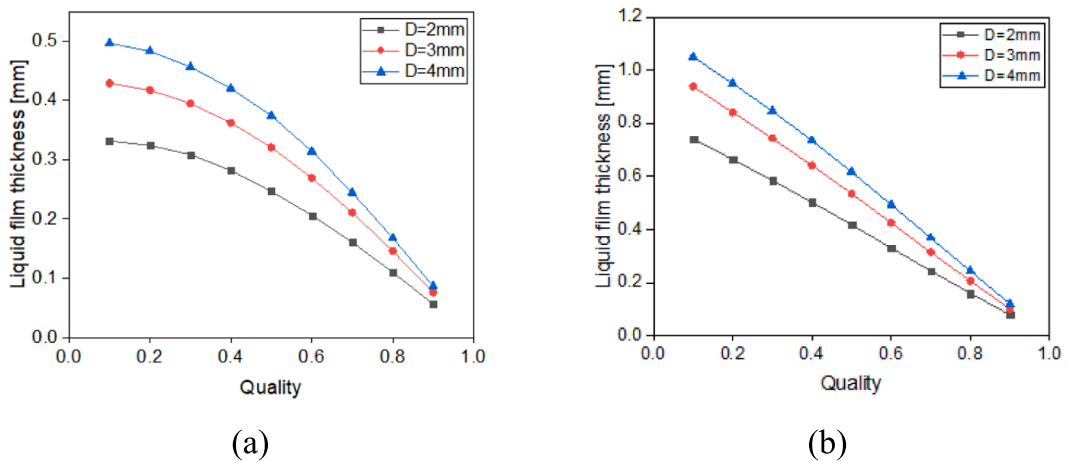


Fig. 11. Liquid-film thickness for different channel diameters: (a) top and (b) bottom.

mass flux increases as it causes the gas velocity (u_g) to increase, which in turn increases the shear force ($u_g \propto \tau$). The elevated shear force progressively reduces the liquid film thickness. Fig. 8 shows the trends of the shear, surface, and gravitational forces acting on the liquid film. Evidently, the shear force increases as the mass flux increases, thereby

resulting in a thinner liquid film ($\tau \propto 1/\delta$), which corresponds with the findings of a previous study [30]. Additionally, as the quality reduces, the shear force reduces whereas the surface force increases. This occurs because the decrease in the gas volume at lower levels results in a decreased interfacial shear force and higher surface force owing to the

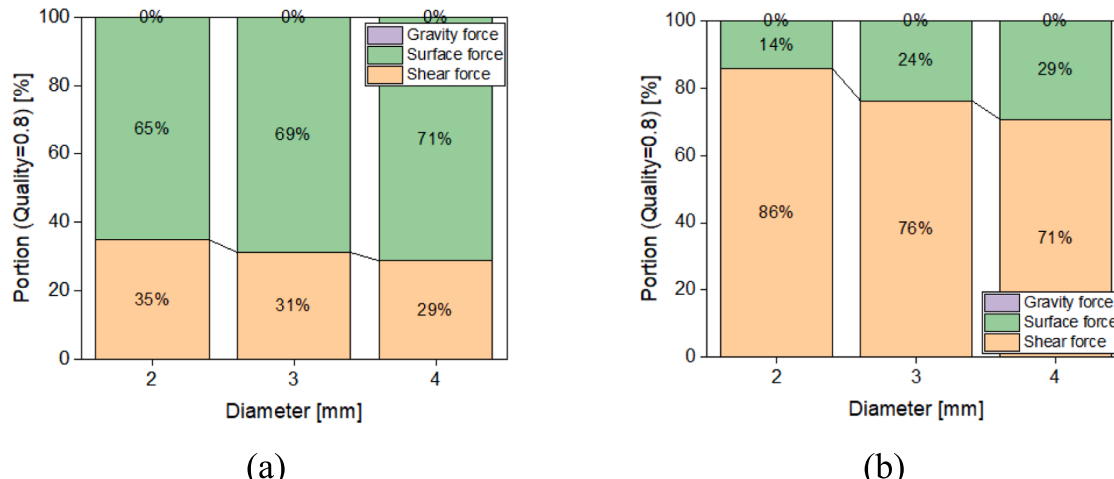


Fig. 12. Variation in forces under different channel diameters: (a) top and (b) bottom.

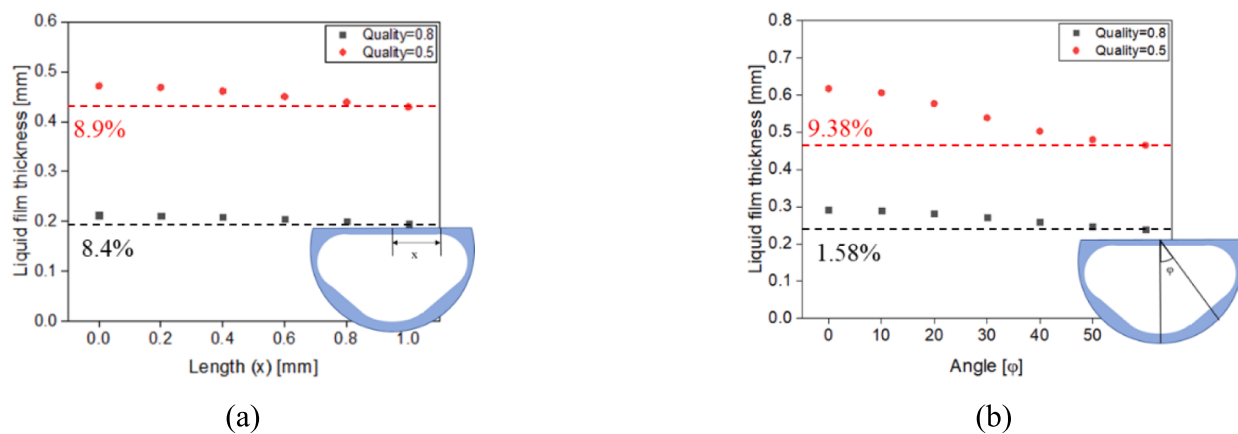


Fig. 13. Liquid film thickness at different positions: (a) top and (b) bottom.

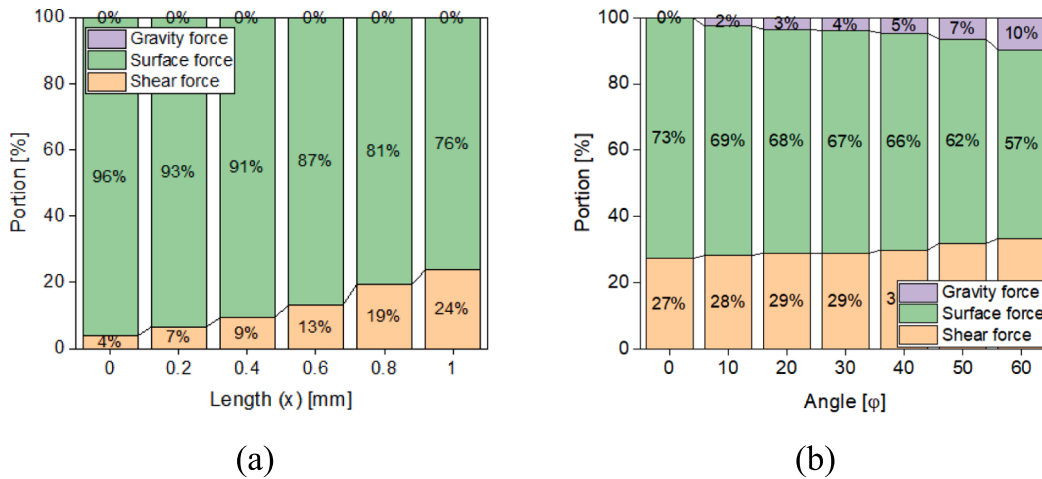


Fig. 14. Portion of forces acting at different positions for a quality of 0.5: (a) top and (b) bottom.

increased liquid film thickness.

5.2. Effect of pressure on liquid film

Fig. 9 illustrates the variation in the liquid film thickness with saturation pressure, which decreases as the saturation pressure

decreases. This behavior is attributed to changes in the CO₂ properties, such as the gas density and surface tension, which are influenced by pressure [31]. Appendix B. shows the pressure-dependence CO₂ properties. As the pressure decreases, the CO₂ gas density decreases, whereas the surface tension increases. The reduced gas density increases the gas velocity (u_g) under similar mass flux conditions, thereby resulting in a

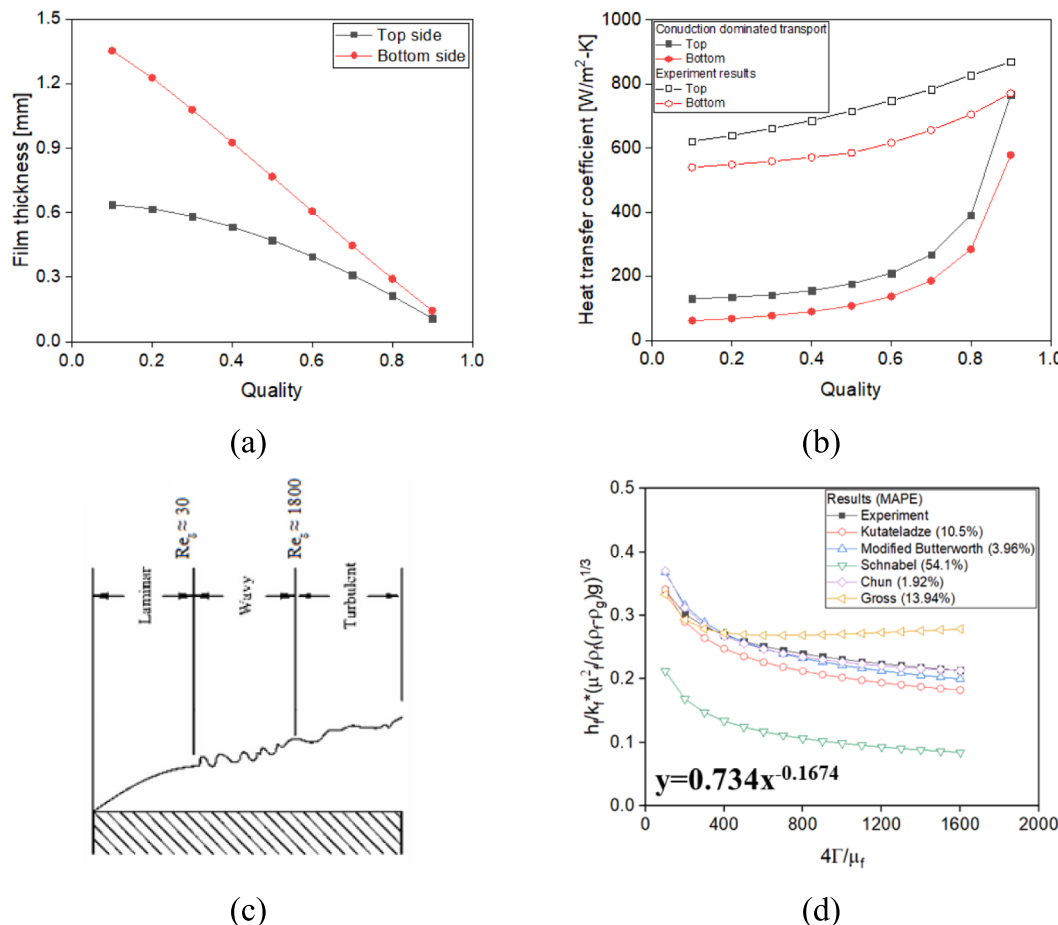


Fig. 15. Relationship between liquid film thickness and heat transfer coefficient: (a) liquid film, (b) conduction dominant transport, (c) flow regimes of liquid film [37], and (d) convection dominant transport.

higher shear force ($u_g \propto \tau$). Simultaneously, an increase in the surface tension promotes uniform liquid film distribution along the radial direction, thereby reducing the liquid film thickness at the [32]. Hence, decreasing the saturation pressure enhances the surface and shear forces, thereby thinning the liquid film at the central points of the top and bottom regions.

Fig. 10 shows the forces as a function of pressure, thereby revealing that the surface force increases as the saturation pressure decreases. While the shear and surface forces increase as the pressure decreases, the surface force exhibits a higher increase rate than the shear force, as shown in Appendix C.. Therefore, the change in liquid film thickness with pressure is more significantly influenced by surface tension under low mass flux conditions (40–80 kg/m²·s).

5.3. Effect of channel diameter on liquid film

Fig. 11 shows the influence of channel diameter on the liquid film thickness. As the diameter decreases, the liquid film becomes thinner. Smaller channels exhibit a lower Reynolds number under similar mass flux conditions ($Re = G^*D_h/\mu$). The decrease in the Reynolds number increases the friction factor ($f \propto 1/Re$), thereby increasing the shear force ($f \propto \tau$) and reducing the liquid film. In addition to the shear force effect, numerous studies have shown that smaller channels increase the

surface force effects [33], thereby resulting in a thinner liquid film at the center. While the shear and surface forces increase as the diameter decreases (Appendix C.), the shear force increases at a faster rate. Hence, the relative contribution of the shear force increases as the diameter decreases, as illustrated in Fig. 12.

6. Discussion

6.1. Effect of positions on the liquid film

Fig. 13(a) shows the liquid film distribution along the top of the channel, wherein it is thickest at the center and tends to decrease as the distance from the center increases, which corresponds with findings from previous studies [34,35]. However, the variation in the liquid film thickness along the top is relatively small, less than approximately 8 %. As shown in Fig. 14(a), the surface force decreases as the distance from the center increases. Hence, as the surface force at the center is the highest, the mass flow rate in the x-direction from the center must be large, thereby indicating that the liquid film must be thin at the center. However, it is the thickest at the center. Appendix D. shows the mass flow rates based on the position, thereby indicating that the mass condenses owing to the high heat flux at the center exceeds that moving in the x-direction from the center owing to the surface force. Consequently,

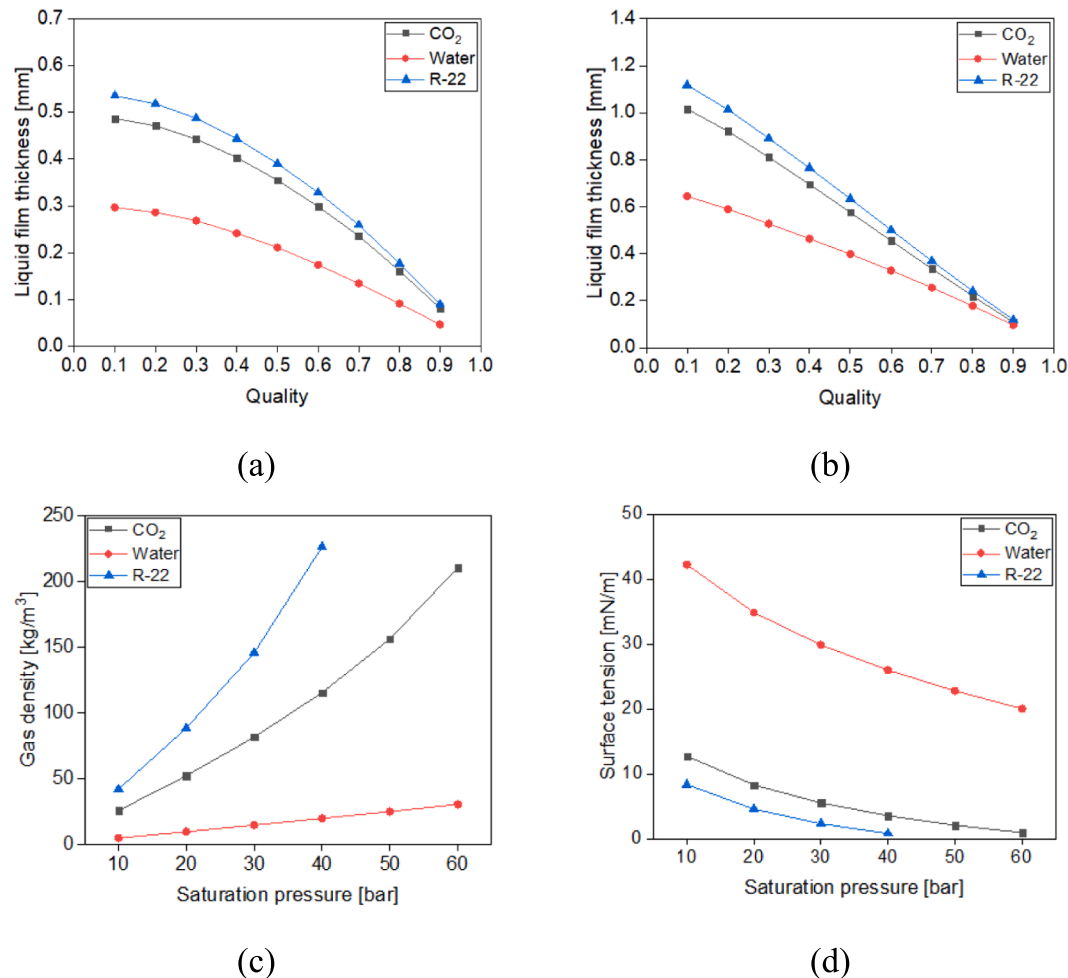


Fig. 16. Liquid film thickness under different working fluids: (a) top and (b) bottom. Properties under varying (c) gas density and (d) surface tension.

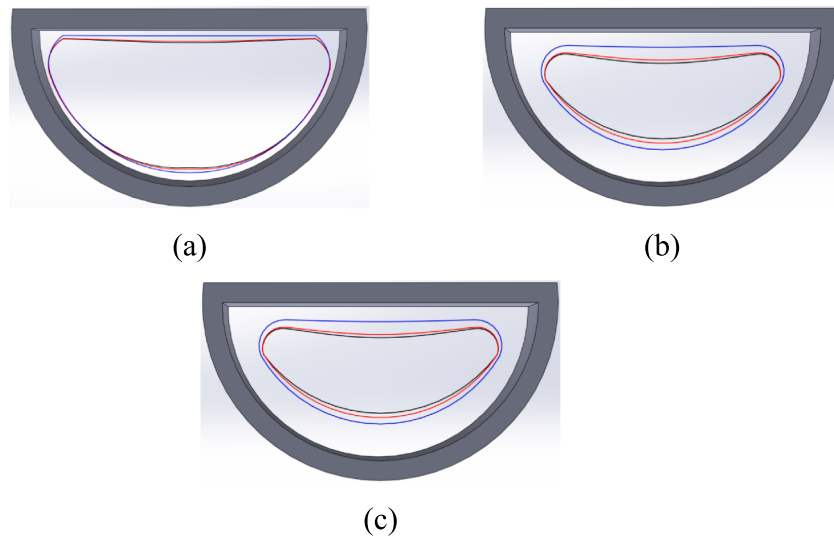
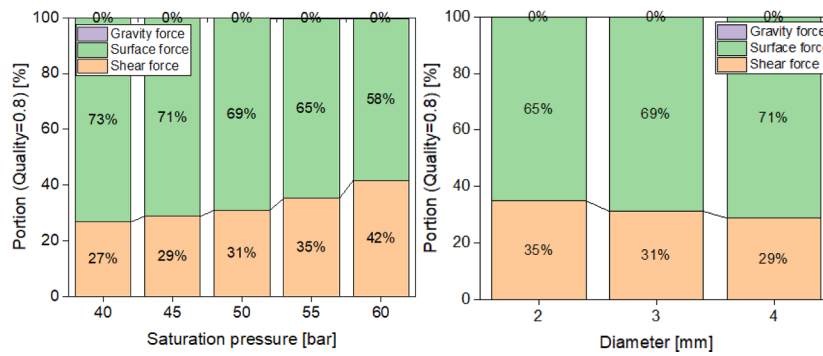


Fig. 17. Structures of liquid films formed using CO₂ (Red), water (Blue), and R-22 (Black) under qualities of (a) 0.9, (b) 0.7, and (c) 0.5.

the liquid film is thicker at the center.

Fig. 13(b) shows the liquid film distribution at the bottom of the channel as a function of the angle, wherein a similar trend as that in the top region can be observed. Under high-quality conditions (quality =

0.8), the liquid film is nearly uniform in the radial direction. However, as the quality decreases, the liquid film becomes thickest at the center (angle = 0) and thins as the angle increases. This is because the mass condensed at the center is greater than that flowing away in the radial



direction owing to the surface force, as shown in Appendix D.. Further, the influence of gravitational force increases as the angle increases, thereby driving the liquid film to the center. However, the effect of the gravitational force is lower than that of the shear and surface forces owing to the small mass of the thin liquid film in the minichannels.

These findings suggest that even with a small channel diameter in the PCHE, the heat transfer coefficient at the bottom is likely to be lower than that at the top owing to of the thicker liquid film at the bottom. Hence, the heat transfer performance of the PCHE can be enhanced by increasing the number of cold channels under the hot channels to facilitate heat exchange.

6.2. Relationship between liquid film and heat transfer coefficient

To analyze the heat transfer characteristics of the liquid film, a correlation between the liquid film thickness and heat transfer coefficient was developed. Fig. 15(a) shows the liquid film thickness calculated using the model developed for the top and bottom regions. According to the model developed by Nusselt [11], heat transfer in the liquid film occurs primarily via conduction under laminar flow conditions. Fig. 15(b) compares the heat transfer coefficients (filled symbols) calculated using Nusselt's assumption ($\mathbf{h} = k/\delta$) and those obtained experimentally, thereby indicating considerable differences between both. These differences are noticeable under all quality conditions, except at very high qualities. As per a previous study, the critical Reynolds number for transitioning from laminar to wavy-laminar flows is 30 [36], as shown in Fig. 15(c). At very high-quality conditions ($x = 0.98-1$), the liquid film is considerably thin and laminar, thereby resulting to heat transfer via conduction. However, a wavy-laminar flow develops when the Reynolds number of the liquid film in the PCHE is 20 or higher. This indicates that the transition from laminar to wavy-laminar flow occurs earlier in PCHEs owing to the considerable influence of the interfacial shear force in the minichannels. Consequently, the heat transfer coefficient must be predicted using the conduction dominated model under laminar flow conditions when the Reynolds number of the liquid film is below 20. Hence, establishing a relationship between the liquid film and heat transfer coefficient becomes challenging the using the when the Reynolds number of liquid film exceeds 20, as the conduction-dominated transport no longer applies.

Seban and Churn [37] observed that waves were formed even in thin liquid films and experimentally derived a correlation between the liquid film and heat transfer coefficient under wavy-laminar flow conditions. The majority of the experimental results in this study indicate the

presence of wavy-laminar flow, as shown in Appendix F.. Fig. 15(d) compares the correlations obtained using the proposed model (filled symbols) to those developed in previous studies (empty symbols) [36] for wavy-laminar flow. The correlation developed in herein shows an MAPE of approximately 1–13 % compared to earlier models, thereby demonstrating that the liquid film in the PCHE is predominantly formed through a wavy-laminar flow and transferred via convection.

6.3. Effects of working fluid properties on liquid film

To analyze the effects of the working fluid properties on the liquid film, its thickness at the top and bottom regions was calculated for different working fluids under similar conditions, as shown in Fig. 16(a) and (b), respectively. R-22 forms the thickest film, whereas water forms the thinnest. This can be attributed to differences in their physical properties, as shown in Fig. 16(c) and (d), which present the results under varying gas densities and surface tensions, respectively. The lower the gas density, the higher the velocity of gas when the mass flux is constant, thereby resulting in a higher shear force and consequently thinner liquid films. Hence, water, which has the lowest gas density, forms the thinnest film. In addition to the effect of density, the liquid film is affected by surface tension. As presented in Section 5.2, a larger surface force results in a higher mass flow rate in the x-direction at the top or r-direction at the bottom. Because the surface tension of water is the highest among the fluids employed in this study, its liquid film is the thinnest. In other words, a large surface force resulting in an even liquid-film distribution, as shown in Fig. 17.

The liquid film thickness affects the heat transfer coefficient. A previous study [19] compared the heat-transfer coefficients of different working fluids in a PCHE. Although the two heat-transfer coefficients are similar, the heat transfer coefficient of CO₂ tends to be slightly higher than that of R-22 under similar, as shown in Appendix G.. This difference is attributed to variations in the liquid film distribution owing to the distinct properties of R-22 and CO₂.

7. Conclusion

In this study, we developed a theoretical liquid-film model of a PCHE with a semicircular channel using governing equations such as conservation, momentum, and energy. This model was employed to analyze the liquid film behavior under varying channel diameters, mass fluxes, and saturation pressures. The key findings of this study are summarized as follows:

- (1) The validity of the proposed model was confirmed via comparisons with conventional void fraction models. The predictions of the Wallis void fraction model corresponded with those of the proposed model, with an MAPE of approximately 9.9 %. Additionally, the liquid film distribution predicted using the proposed model corresponded with that obtained via VOF simulations, with a difference of approximately 7.4 %.
- (2) The liquid film thickness decreased with an increase in the mass flux because the portion of the shear force in the total forces increased from 42 % to 89 % owing to an increase in the gas velocity. Further, the liquid film thickness decreased with the decreasing channel diameter as the shear force increased from 29 % to 35 % owing to a decrease in the Reynolds number. A decrease in the saturation pressure reduced the liquid film thickness, as lower pressure resulted in a decrease in the gas density, thereby increasing the gas velocity and shear force. Additionally, the corresponding increase in the surface tension contributed to a more uniform liquid film distribution, thereby resulting in a thinner film at the center. Although both forces increase as the pressure decreased, the effect of the surface force increased from 58 % to 73 % because the increase rate in surface force was larger than that in shear force.
- (3) The liquid film distribution varied across different regions. At the top, the difference in the film thickness was relatively uniform (approximately 8.9 %) owing to the considerable influence of the surface tension, which drove liquid from the center toward the edges in the x-direction. Conversely, the film thickness at the bottom side varied significantly with the angle (approximately 9.4 %), as the effect of the surface tension was relatively small in this region, with liquid moving toward the center under gravitational force.
- (4) To understand the heat transfer mechanism of the liquid film, we analyzed whether it was dominated by conduction or convection. In the case of conduction-dominant transport, the difference between the heat-transfer coefficients predicted by the model and those obtained experimentally was significant. Conversely, in the

case of the convection-dominant transport, the values exhibited an MAPE of approximately 1–14 % compared with existing models and were accurately predicted. This indicated that the liquid film exhibited wavy-laminar flow characteristics, with heat transfer primarily occurring via convection.

- (5) The liquid films formed using water, a refrigerant (R-22), and CO₂ were compared. Water resulted in the thinnest film, whereas the refrigerant resulted in the thickest film. This was attributed to the differences in their physical properties, such as surface tension and density. Low-density water has a higher gas velocity, thereby resulting in a higher shear force and approximately 20–30 % thinner films than CO₂. Additionally, the high water surface tension enhanced the surface force, thereby causing it to flow in the x- or r-directions and resulting in a liquid film that was thin at the center.

Declaration of competing interest

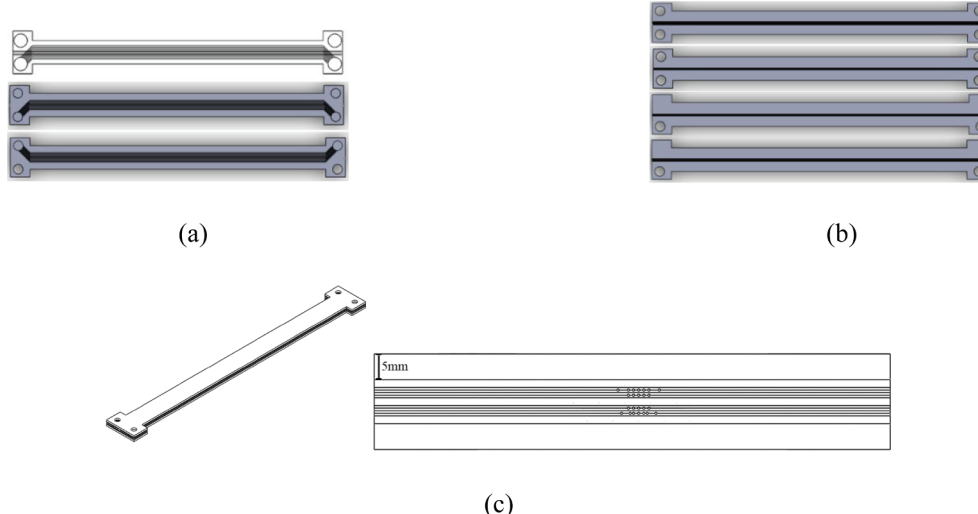
The authors declare that they have no known competing financial interests or personal relationships that could have appeared to influence the work reported in this paper.

Acknowledgement

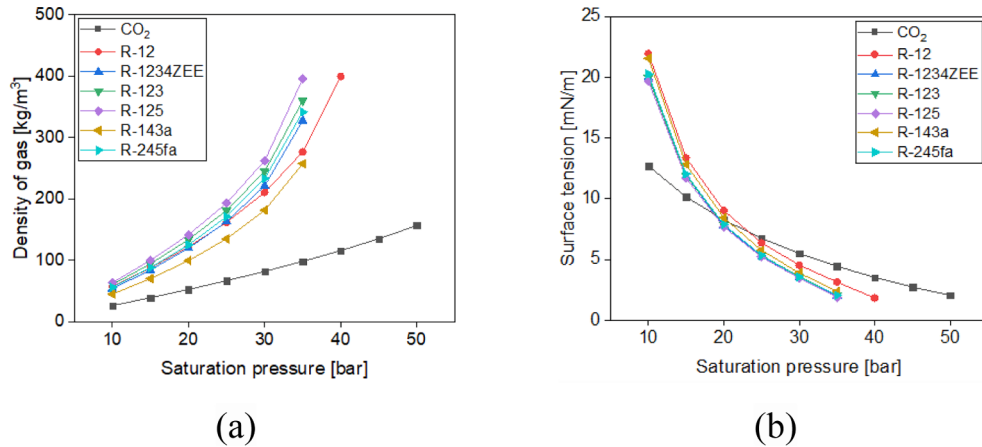
Funding.

This research was supported by Pohang Iron & Steel Company (POSCO) Holdings (2024Q006) and Korea Institute of Energy Technology Evaluation and Planning (KETEP) grant funded by the Korean government (MOTIE). (20222020800130, Development and demonstration of hybrid power system using ORC (Organic Rankine Cycle) and TEG (Thermoelectric Generator) for low and medium temperature industrial waste heat recovery).

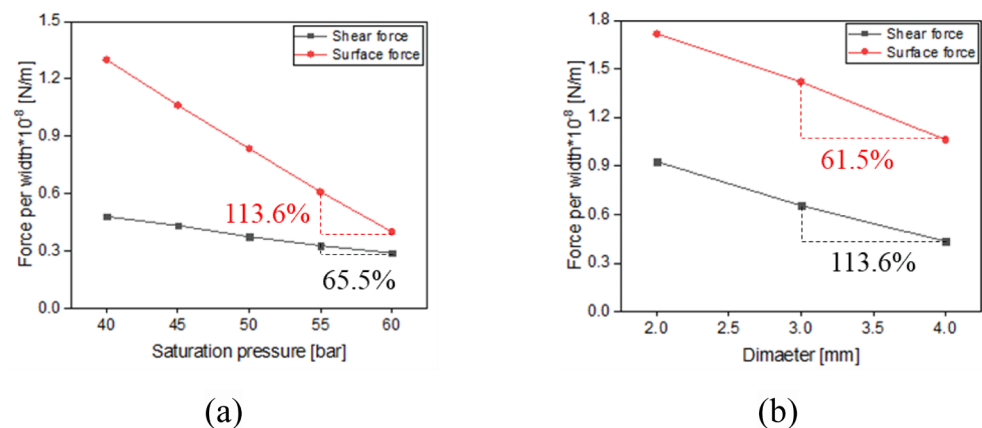
Appendix A. Illustrations of the (a) hot and cold plates, (b) OFS plates, and (c) PCHE

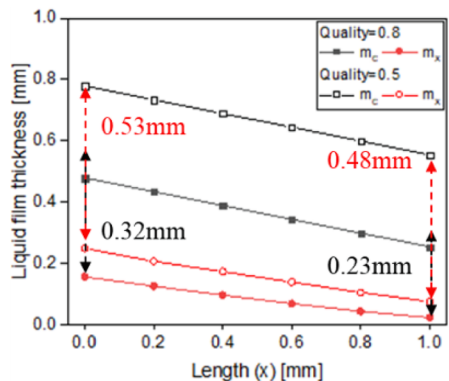


Appendix B. Properties of the working fluids under different saturation pressures: (a) density of the gas phase (b) surface tension

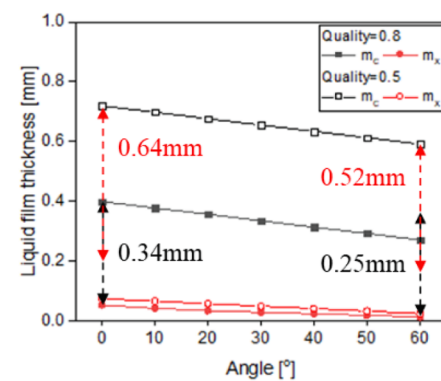


Appendix C. Change in forces according to (a) saturation pressure and (b) channel diameter

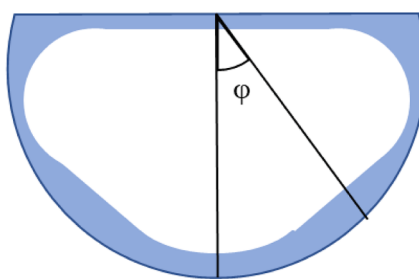


Appendix D. Liquid film thickness: (a) top and (b) bottom


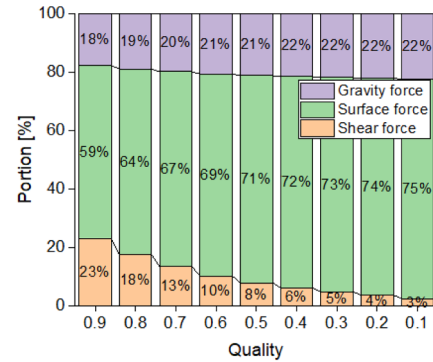
(a)



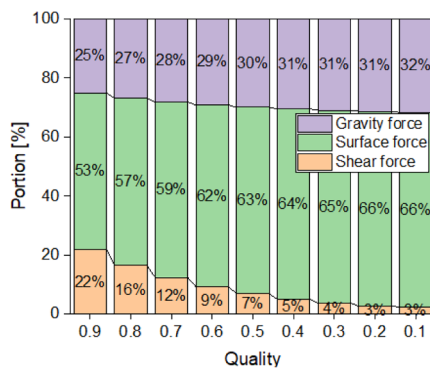
(b)

Appendix E. Force portion at (a) position and angles of (b) 30° (c) 45° and (d) 60°


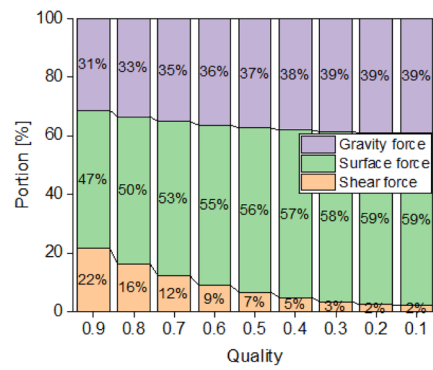
(a)



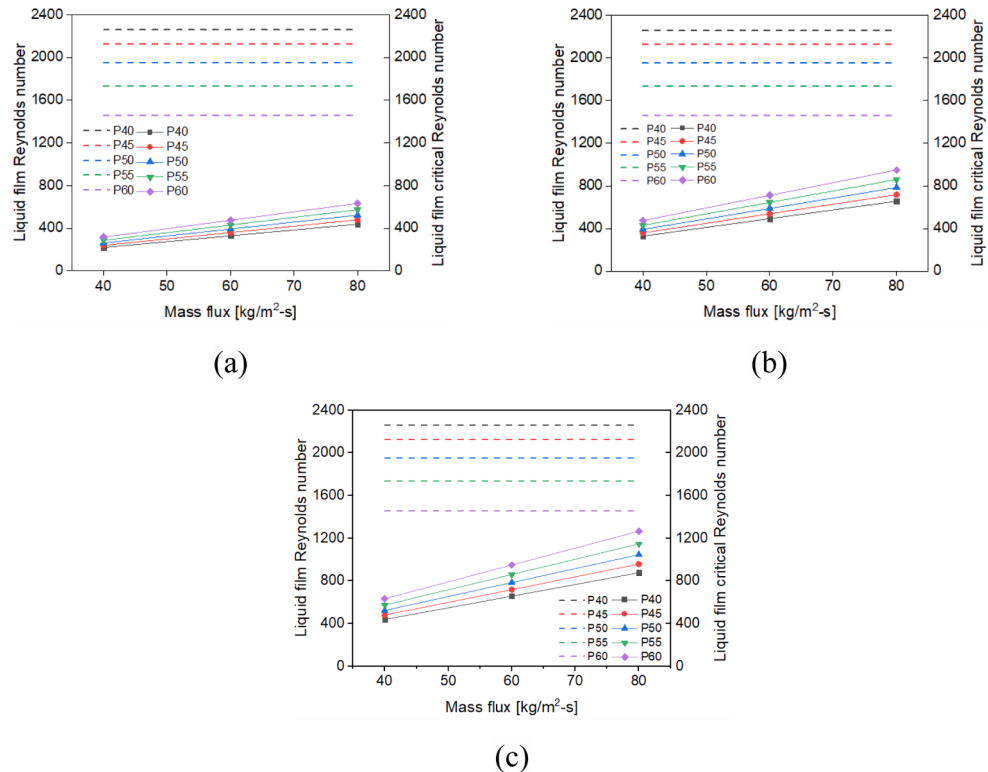
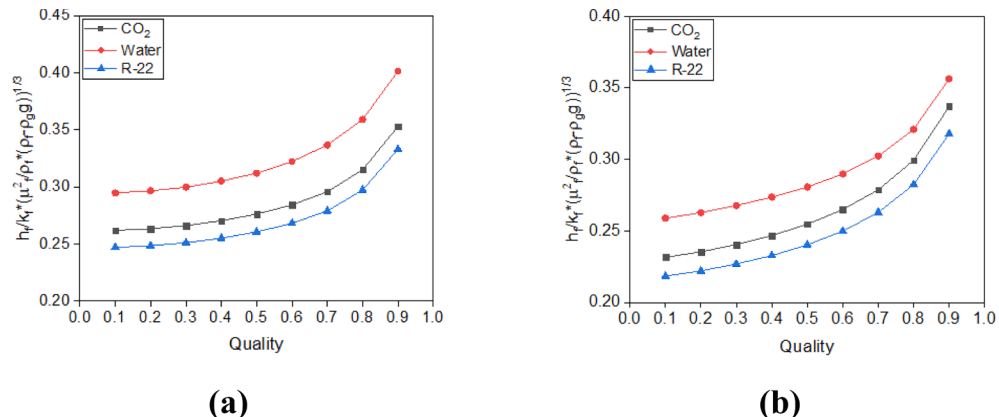
(b)



(c)



(d)

Appendix F. Flow patterns of the liquid film. D= (a) 2, (b) 3, and (c) 4 mm

Appendix G. Heat-transfer coefficients for different working fluids: (a) top and (b) bottom

Data availability

Data will be made available on request.

References

- [1] Na. Zhang, et al., COOLCEP (cool clean efficient power): A novel CO₂-capturing oxy-fuel power system with LNG (liquefied natural gas) coldness energy utilization, *Energy* 35 (2) (2010) 1200–1210.
- [2] Kanbur, Baris Burak, et al. “Cold utilization systems of LNG: A review.” *Renewable and sustainable energy reviews* 79 (2017): 1171-1188.

- [3] LEE, JIHWAN, and JUNGHO CHO. "Estimation of the Amount of Electric Power Saved in the Carbon Dioxide Liquefaction Process using LNG Cold Heat." Transactions of the Korean hydrogen and new energy society 31.2 (2020): 259-264.
- [4] C. Li, L. Pan, Y. Wang, Thermodynamic optimization of Rankine cycle using CO₂-based binary zeotropic mixture for ocean thermal energy conversion, *Appl. Therm. Eng.* 178 (2020) 115617.
- [5] L. Tang, Z. Cao, J. Pan, Investigation on the thermal-hydraulic performance in a PCHE with airfoil fins for supercritical LNG near the pseudo-critical temperature under the rolling condition, *Appl. Therm. Eng.* 175 (2020) 115404.
- [6] Z. Zhao, et al., Effect of different zigzag channel shapes of PCHEs on heat transfer performance of supercritical LNG, *Energies* 12 (11) (2019) 2085.
- [7] T. He, et al., LNG cold energy utilization: Prospects and challenges, *Energy* 170 (2019) 557-568.
- [8] D. Kwon, et al., Experimental investigation of heat transfer coefficient of mini-channel PCHE (printed circuit heat exchanger), *Cryogenics* 92 (2018) 41-49.
- [9] J.W. Yoo, C.W. Nam, S.H. Yoon, Experimental study of propane condensation heat transfer and pressure drop in semicircular channel printed circuit heat exchanger, *Int. J. Heat Mass Transf.* 182 (2022) 121939.
- [10] Z.-R. Peng, Q.-Y. Zheng, X.-R. Zhang, Numerical study of condensation process in semi-circular mini-channels for the printed circuit heat exchanger, *Heat Transfer Eng.* 43 (8-10) (2022) 785-793.
- [11] W. Nusselt, Die oberflachenkondensation des wasserdampfes, VDI-Zs 60 (1916) 541.
- [12] J. Wen, et al., Effect of surface tension, gravity and turbulence on condensation patterns of R1234ze (E) in horizontal mini/macro-channels, *Int. J. Heat Mass Transf.* 125 (2018) 153-170.
- [13] S.M. Kim, I. Mudawar, Theoretical model for annular flow condensation in rectangular micro-channels, *Int. J. Heat Mass Transf.* 55 (4) (2012) 958-970.
- [14] Y. Ding, et al., Theoretical investigation on convective condensation annular flow of R410a inside rectangular microchannel, *Int. J. Heat Mass Transf.* 131 (2019) 698-708.
- [15] J.i. Wang, J.M. Li, Y. Hwang, Modeling of film condensation flow in oval microchannels, *Int. J. Heat Mass Transf.* 126 (2018) 1194-1205.
- [16] Y. Liu, et al., Numerical investigation on the condensation of R134a, R1234ze (E) and R450A in mini-channels, *Int. J. Refrig.* 130 (2021) 305-316.
- [17] L.S. Won, et al., Condensation heat transfer and applicability assessment of a printed circuit heat exchanger as a condenser in a cryogenic CO₂ capture and storage system, *Appl. Therm. Eng.* (2024) 125133.
- [18] P. Toninelli, et al., Effects of geometry and fluid properties during condensation in minichannels: experiments and simulations, *Heat Mass Transf.* 55 (2019) 41-57.
- [19] M. Matkovic, et al., Experimental study on condensation heat transfer inside a single circular minichannel, *Int. J. Heat Mass Transf.* 52 (9-10) (2009) 2311-2323.
- [20] Wang, Hua Sheng, and John W. Rose. "A theory of film condensation in horizontal noncircular section microchannels." (2005): 1096-1105.
- [21] Zhao, T. S., and Qiang Liao. "Theoretical analysis of film condensation heat transfer inside vertical mini triangular channels." *International journal of heat and mass transfer* 45.13 (2002): 2829-2842.
- [22] K. Keniar, B. El Fil, S. Garimella, A critical review of analytical and numerical models of condensation in microchannels, *Int. J. Refrig.* 120 (2020) 314-330.
- [23] Wang, Huasheng, and John W. Rose. "Film condensation in horizontal microchannels: effect of channel shape." *International Conference on Nanochannels, Microchannels, and Minichannels*. Vol. 41855. 2005.
- [24] P. Roriz, et al., Optical fiber temperature sensors and their biomedical applications, *Sensors* 20 (7) (2020) 2113.
- [25] L.S. Won, et al., "Evaluation of thermal-hydraulic performance and economics of printed circuit heat exchanger (PCHE) for recuperators of sodium-cooled fast reactors (SFRs) using CO₂ and N₂ as working fluids.", *Nuclear Eng. Technol.* 54 (5) (2022) 1874-1889.
- [26] D. Tombe Bas, B. Schilperoort, M. Bakker, Estimation of temperature and associated uncertainty from fiber-optic raman-spectrum distributed temperature sensing, *Sensors* 20 (8) (2020) 2235.
- [27] J. Winkler, et al., Void fractions for condensing refrigerant flow in small channels: Part I literature review, *Int. J. Refrig.* 35 (2) (2012) 219-245.
- [28] J. Winkler, J. Killion, S. Garimella, Void fractions for condensing refrigerant flow in small channels. Part II: Void fraction measurement and modeling, *Int. J. Refrig.* 35 (2) (2012) 246-262.
- [29] H.R. Kopke, Experimental investigation of void fraction during refrigerant condensation in horizontal tubes, *Air Conditioning and Refrigeration Center TR-142* (1998).
- [30] Da Riva, E., and Davide Del Col. "Numerical simulation of laminar liquid film condensation in a horizontal circular minichannel." (2012): 051019.
- [31] A.O. Adelaja, J. Dirker, J.P. Meyer, Experimental study of the pressure drop during condensation in an inclined smooth tube at different saturation temperatures, *Int. J. Heat Mass Transf.* 105 (2017) 237-251.
- [32] S. Bortolin, E. Da Riva, D. Del Col, Condensation in a square minichannel: application of the VOF method, *Heat Transfer Eng.* 35 (2) (2014) 193-203.
- [33] P. Toninelli, et al., Visualization and numerical simulations of condensing flow in small diameter channels, *Heat Transfer Eng.* 40 (9-10) (2019) 802-817.
- [34] S. Chen, et al., Simulation of condensation flow in a rectangular microchannel, *Chem. Eng. Process.* 76 (2014) 60-69.
- [35] Z. Liu, B. Sundén, J. Yuan, Numerical simulation of condensation in a rectangular minichannel using VOF model. ASME International Mechanical Engineering Congress and Exposition, American Society of Mechanical Engineers, 2012.
- [36] V. Guichet, H. Jouhara, Condensation, evaporation and boiling of falling films in wickless heat pipes (two-phase closed thermosyphons): A critical review of correlations, *International Journal of Thermofluids* 1 (2020) 100001.
- [37] L. Zhao, B. Guo, Z. Yang, An experimental investigation on the evaporation and condensation heat transfer of air-cooled multi-port flat heat pipes, *Int. J. Heat Mass Transf.* 187 (2022) 122554.